Digital holography of total internal reflection

William M. Ash III[*] **and Myung K. Kim**

Digital Holography and Microscopy Laboratory, Dept. of Physics, University of South Florida, Tampa, FL 33620
[*]*Corresponding author: wash@mail.usf.edu*

Abstract: We introduce a new microscopy technique termed total internal reflection holographic microscopy (TIRHM). Quantitative phase microscopy by digital holography is used to image the phase profile of light in total internal reflection, which is modulated by the materials present on or near the surface of internal reflection. The imaging characteristics are theoretically modeled and imaging capabilities are experimentally demonstrated.

©2008 Optical Society of America

OCIS codes: (090.1995) Digital holography; (180.3170) Interference microscopy; (170.0180) Microscopy; (090.5694) Real-time holography; (110.0180) Microscopy; (170.1530) Cell Analysis; (260.6970) Total Internal Reflection

References and links

1. W. Jueptner and U. Schnars, *Digital Holography*, (Springer Verlag, 2004).
2. J. W. Goodman, *Introduction to Fourier Optics*, 2nd ed (New York, McGraw-Hill, 1996).
3. U. Schnars and W.P. Jueptner, "Direct recording of holograms by a CCD target and numerical reconstruction," Appl. Opt. **33**, 179-81 (1994).
4. S. Grilli, P. Ferraro, S. De Nicola, A. Finizio, G. Pierattini and R. Meucci, "Whole optical wavefields reconstruction by digital holography," Opt. Express **9**, 294-302 (2001).
5. I. Yamaguchi and T. Zhang, "Phase-shifting digital holography," Opt. Lett. 22, 1268 (1997).
6. T.-C. Poon, "Three-dimensional image processing and optical scanning holography," Adv. Imaging and Electron Phys. **126**, 329-350 (2003).
7. E. Cuche, F. Bevilacqua and C. Depeursinge, "Digital holography for quantitative phase-contrast imaging," Opt. Lett. **24**, 291 (1999).
8. F. Dubois, C. Schockaert, N. Callens, and C. Yourassowsky, "Focus plane detection criteria in digital holography microscopy by amplitude analysis," Opt. Express **14**, 5895-5908 (2006).
9. P. Ferraro, S. De Nicola, A. Finizio, G. Coppola, S. Grilli, C. Magro and G. Pierattini, "Compensation of the inherent wave front curvature in digital holographic coherent microscopy for quantitative phase-contrast imaging," Appl. Opt. **42**, 1938-46 (2003).
10. M. L. Xu, X. Peng, J. Miao, and A. Asundi, "Studies of digital microscopic holography with applications to microstructure testing," Appl. Opt. **40**, 5046-5051 (2001).
11. G. Pedrini and H. J. Tiziani, "Quantitative evaluation of two-dimensional dynamic deformations using digital holography," Opt. Laser Technol. **29**, 249–256 (1997).
12. W. Xu, M. H. Jericho, I. A. Meinertzhagen, and H .J. Kreuzer, "Digital in-line holography for biological applications," Proc. Natl. Acad. Sci. USA **98**, 11301-05 (2001).
13. K. J. Chalut, W. J. Brown, and A. Wax, "Quantitative phase microscopy with asynchronous digital holography," Opt. Express **15**, 3047-3052 (2007).
14. D. Carl, B. Kemper, G. Wernicke, and G. von Bally, "Parameter-optimized digital holographic microscope for high-resolution living-cell analysis," Appl. Opt. **43**, 6536-6544 (2004).
15. K. Jeong, J. J. Turek, and D. D. Nolte, "Fourier-domain digital holographic optical coherence imaging of living tissue," Appl. Opt. **46**, 4999-5008 (2007).
16. M. K. Kim, "Tomographic three-dimensional imaging of a biological specimen using wavelength-scanning digital interference holography," Opt. Express **7**, 305-10 (2000).
17. L. Yu and M. K. Kim, "Wavelength-scanning digital interference holography for tomographic 3D imaging using the angular spectrum method," Opt. Lett. **30**, 2092-2094 (2005).
18. J. Gass, A. Dakoff and M. K. Kim, "Phase imaging without 2-pi ambiguity by multiwavelength digital holography," Opt. Lett. **28**, 1141-3 (2003).
19. C. J. Mann, L. Yu, C. M. Lo, and M. K. Kim, "High-resolution quantitative phase-contrast microscopy by digital holography," Opt. Express **13**, 8693-8698 (2005).
20. C. Mann, L. Yu, and M. K. Kim, "Movies of cellular and sub-cellular motion by digital holographic microscopy," Biomed. Eng. Online, **5**, 21 (2006).

21. D. Axelrod, "Cell-substrate contacts illuminated by total internal reflection fluorescence," J Cell Biol **89**, 141-145 (1981).
22. D. Axelrod, N. L. Thompson, and T. P. Burghardt, "Total internal reflection fluorescent microscopy," J Microsc **129**, 19-28 (1983).
23. A. S. G. Curtis, "The mechanism of adhesion of cells to glass – a study by interference reflection microscopy," J Cell Biol. **20**, 199-215 (1964).
24. H. Verschueren, "Interference reflection microscopy in cell biology: methodology and applications," J Cell Sci. **75**, 279-301 (1985).
25. W. M. Ash III and M. K. Kim, "A demonstration of total internal reflection holographic microscopy for the study of cellular motion," in *Digital Holography and Three-Dimensional Imaging*, Opt. Soc. Am. Topical Meeting (St. Petersburg, FL, March 2008) Technical Digest.
26. S. De Nicola, A. Finizio, G. Pierattini, P. Ferraro, and D. Alfieri, "Angular spectrum method with correction of anamorphism for numerical reconstruction of digital holograms on tilted planes," Opt. Express **13**, 9935-9940 (2005).

1. Introduction

In digital holography [1], the holographic interference pattern is optically generated by the superposition of object and reference waves. But, instead of a photographic plate, the hologram is digitally sampled by a CCD camera and transferred to a computer as an array of numbers. The propagation of optical field is completely and accurately described by diffraction theory, which allows for numerical reconstruction of the image as an array of complex numbers representing the amplitude and phase of the optical field [2]. Digital holography offers a number of important advantages such as the ability to acquire images rapidly, the availability of both amplitude and phase information of the optical field, and versatility of the image processing techniques that can be applied to the complex field data. Indeed, digital holography by numerical diffraction of optical fields allows for imaging and image processing techniques that are not feasible in real space holography. Schnars and Jueptner, in 1994, were the first to use a CCD camera connected to a computer as the input, in what is now referred to as digital holography [3]. Since then, developments of digital holographic techniques and applications have been gaining pace ever more rapidly. A number of different methods have been considered for numerical reconstruction including the Fresnel transform, the Huygens convolution, and angular spectrum analysis [4]. Various useful and special techniques have been developed to enhance the capabilities and to extend the range of applications. Phase-shifting digital holography allows the elimination of zero-order and twin-image components even in an on-axis arrangement [5]. Optical scanning holography can generate holographic images of fluorescence [6]. Application of digital holography in microscopy is especially important, because of the very narrow depth of focus of high-magnification systems [7]. Numerical focusing of holographic images can be accomplished from a single hologram [8]. Direct access to the phase information facilitates numerical correction of various aberrations of the optical system, such as field curvature and anamorphism [9]. Digital holography has been particularly useful in metrology, deformation measurement, particle analysis, and vibrational analysis [10,11]. Applications of digital holography for biological microscopy are being actively pursued [12-14]. Low-coherence digital holography allows tomographic imaging [15]. Our laboratory has developed digital interference holography for optical tomographic imaging [16,17] as well as multiwavelength phase contrast digital holography for high resolution microscopy [18-20].

In 1981, D. Axelrod [21, 22] demonstrated total internal reflection fluorescence microscopy (TIRFM) to be an effective technique to study cell-substrate contact. When light is incident from inside of a higher-index medium n_1 into a lower-index one n_2, with the angle of incidence greater than the critical angle $\theta_c = \sin^{-1}(n_2/n_1)$, all of the incident light is reflected back to the first medium. There is no propagating field in the second medium, except for the evanescent wave, whose amplitude decays exponentially over a distance of a fraction of a wavelength. Although the evanescent field is non-propagating, it can be made to give off propagating, and therefore detectable, radiation through a number of processes: i) If another

n_2 / n_1 interface is brought close to the first n_1 / n_2 interface, then part of the evanescent wave couples into the second n_1 medium and propagates, a process known as frustrated TIR (fTIR). ii) Inhomogeneity in the index n_2 of the second medium can cause scattering of the evanescent field. iii) Suitable dye molecules placed in the evanescent field can absorb energy from the field and give off fluorescence. The process i) is the basis of the near-field scanning optical microscopy, while the process ii) can be used for TIR microscopy of unstained samples and iii) is the TIRFM. In cellular biology, there are many compelling questions involving processes that take place at the cell surface or plasma membrane and it has long been recognized that TIR microscopy can be a powerful tool in answering such questions. Recent technical advances have greatly facilitated a wider range of applications of TIR microscopy. TIRFM imagery reveals localization of fusion protein in cell focal adhesions at the substrate interface in dramatic contrast to the blur produced by out-of-plane fluorescence in the epi-illumination image. Information on the morphology of the cellular membrane surface, however, is largely absent in TIRFM. On the other hand, in interference reflection microscopy (IRM), light waves reflected from two surfaces of the cell-substrate interface produces interference fringes, thus allowing estimation of the interface thickness profile [23,24]. However, with IRM the interference image of the interface is usually complicated by the reflection image of the cell body and its contents, thus allowing only a qualitative interpretation of the surface profile. Confocal adaptation of IRM can reduce the spurious reflection signal, but raster scanning of such a system imposes significant speed limitations.

In this paper, quantitative phase microscopy by digital holography is applied in the imaging of phase profile of light in total internal reflection [25]. The technique, termed total internal reflection holographic microscopy (TIRHM), is based on the realization that the presence of materials on the interface modulates the phase profile of light in total internal reflection. TIRHM imaging makes use of the 'total' internal reflection, meaning that essentially all of the input photons participate in the formation of the image signals, and therefore the input optical power can be kept at minimal level. One can obtain phase images of prism-cell interface with an optical thickness resolution of a few nanometers. We have demonstrated these imaging principles of TIRHM using model objects of liquid droplets and spherical surface of known material and shape, and the results indicate distinct capabilities and potential strengths in biomedical cellular microscopy and other applications.

2. Theory

Consider reflection of light, of vacuum wavelength λ_0, across a boundary between two dielectric media with indices n_1 and n_2. The reflection coefficients are given by the familiar Fresnel equations:

$$r_\perp = \frac{n_1 \cos\theta_1 - n_2 \cos\theta_2}{n_1 \cos\theta_1 + n_2 \cos\theta_2}; \quad r_{//} = \frac{n_2 \cos\theta_1 - n_1 \cos\theta_2}{n_2 \cos\theta_1 + n_1 \cos\theta_2} \tag{1}$$

for the s-polarization ($r_\perp$) and the p-polarization ($r_{//}$), respectively. For internal reflection, $n_1 > n_2$, if the angle of incidence θ_1 is larger than the critical angle $\theta_c = \sin^{-1}(n_2/n_1)$, then the reflectance $R = |r|^2$ becomes unity in total internal reflection (TIR) and $\cos\theta_2$ is imaginary. Defining

$$h_2 = n_2 \cos\theta_2 = i\sqrt{n_1^2 \sin^2\theta_1 - n_2^2} = i\eta_2 , \tag{2}$$

the reflection coefficients become complex:

$$r_\perp = \exp\left(-2i\varphi_\perp\right); \quad \varphi_\perp = \tan^{-1}\frac{\eta_2}{n_1\cos\theta_1} = \tan^{-1}\frac{\sqrt{n_1^2\sin^2\theta_1 - n_2^2}}{n_1\cos\theta_1} \tag{3}$$

$$r_{//} = \exp\left(-2i\varphi_{//}\right); \quad \varphi_{//} = \tan^{-1}\frac{n_1\eta_2}{n_2^2\cos\theta_1} = \tan^{-1}\frac{n_1\sqrt{n_1^2\sin^2\theta_1 - n_2^2}}{n_2^2\cos\theta_1} \tag{4}$$

There is no propagating wave in transmission, but a thin layer of evanescent wave exists that decays exponentially, $E_t \propto \exp\left(-k_0\eta_2 z\right)$, where $k_0 = 2\pi/\lambda_0$ and z is the distance from the interface.
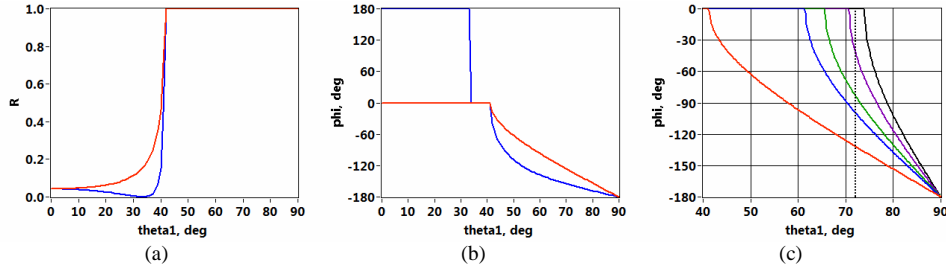

Fig. 1. (a). Reflectance R and (b) reflection phase, phi (φ in text) vs. angle of incidence, theta1 (θ_1 in text) for the relative index, $n_1/n_2 = 1.517$. [red: s-polarization; blue: p-polarization] (c) Reflection phase of s-polarization vs. angle of incidence for various relative indices: $n_1 = 1.517$; $n_2 = 1.000$ (red), 1.333 (blue), 1.382 (green), 1.432 (purple), 1.458 (black).

Figure 1(a) shows the reflectance R = $|r|^2$ vs. angle of incidence θ_1, while Fig. 1(b) is the reflection phase φ vs. θ_1 for the relative index $n_1/n_2 = 1.517$. One notes the Brewster angle at 33° and the critical angle at 41°. While the reflection phase is only zero or 180° for non-TIR Fresnel reflection, beyond the critical angle the reflection phase decreases continuously and monotonically from 0 to −180° for both cases of polarization. Figure 1(c) illustrates the reflection phase of s-polarization for a few values of the relative index, with $n_1 = 1.517$ and $n_2 = 1.000$, 1.333, 1.382, 1.432, and 1.458. Here the n_1 value represents the BK7 glass prism and the n_2 values are for air, water, 50/50 mixture of water and ethylene glycol, pure ethylene glycol, and fused quartz, respectively, which are the materials used in the measurements below. For a given angle of incidence, for example 72° shown as dotted line in Fig. 1(c), the phase of TIR-reflected light will vary with n_2 the index of refraction of the second medium. This suggests one possible mode of TIR imaging, where the phase profile of the TIR-reflected light reveals the variation of index of refraction of material in contact with the prism.

Another imaging mode makes use of the frustrated TIR (fTIR) that occurs when a third layer of index n_3 is brought close to the interface within the thickness of the evanescent wave. (Here we use the term frustrated TIR in a general sense that includes any disturbance, in amplitude or phase, of TIR by the presence of another interface within the evanescent field.) Referring to the geometry of Fig. 2, light is incident from the n_1 medium and undergoes

reflection at the two interfaces n_1/n_2 and n_2/n_3. The reflection coefficient, for s-polarization, is found to be

$$r_\perp = \left(\frac{E_1'}{E_1}\right)_\perp = \frac{(h_1 - h_2)(h_2 + h_3) + (h_1 + h_2)(h_2 - h_3)\exp(2i\varphi_0 h_2)}{(h_1 + h_2)(h_2 + h_3) + (h_1 - h_2)(h_2 - h_3)\exp(2i\varphi_0 h_2)}, \tag{5}$$

where $h_i = n_i \cos\theta_i = \sqrt{n_i^2 - n_1^2 \sin^2\theta_1}$ and $\varphi_0 = k_0 z_0$. For illustration, if we take $n_1 = 1.517$ (glass), $n_2 = 1.000$ (air), and $n_3 = 1.458$ (quartz), then the critical angles for the n_1/n_2 and n_1/n_3 interfaces are $\theta_{c,12} = 41°$ and $\theta_{c,13} = 74°$, respectively.
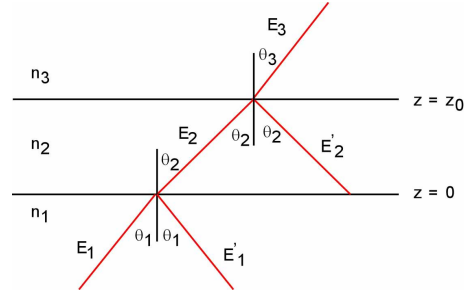

Fig. 2. Geometry of frustrated TIR (fTIR).

The reflectance $R = |r|^2$ and reflection phase φ are graphed in Figs. 3(a) and 3(b), respectively, as two-dimensional functions of the angle of incidence θ_1 and the n_2-layer thickness z_0. Figure 3(c) is an expanded view of the dotted-box area of Fig. 3(b), showing details of the subtle and rapid variation of phase over a short distance of z_0. Figures 3(d) and 3(e) are graphs of $R(z_0)$ and $\varphi(z_0)$, respectively, for several values of θ_1. Figure 3(f) is an expanded view of the dotted-box area of Fig. 3(e). As indicated in Fig. 3, there are three distinct ranges of θ_1 for consideration:

Case I: When $\theta_1 < \theta_{c,12}, \theta_{c,13}$, r is real and both the reflectance and reflection phase display the oscillatory characteristics of thin film interference, as shown in Fig. 3 for $\theta_1 < 41°$.

Case II: When $\theta_{c,12} < \theta_1 < \theta_{c,13}$, the n_1/n_2 interface is in TIR ($h_2 = i\eta_2$ becomes imaginary), but the n_1/n_3 interface is not, and the overall reflection coefficient becomes

$$r_\perp = \left(\frac{E_1'}{E_1}\right)_\perp = \frac{(h_1 - i\eta_2)(i\eta_2 + h_3) + (h_1 + i\eta_2)(i\eta_2 - h_3)\exp(-2\varphi_0 \eta_2)}{(h_1 + i\eta_2)(i\eta_2 + h_3) + (h_1 - i\eta_2)(i\eta_2 - h_3)\exp(-2\varphi_0 \eta_2)}. \tag{6}$$

This is the conventional narrow definition of fTIR, where the evanescent field couples into the third medium and becomes a propagating field. For sufficiently short z_0, a fraction of wavelength, the reflectance is substantially reduced and the reflection phase varies monotonically with z_0, as shown in Fig. 3 for $41° < \theta_1 < 74°$. This is the regime where

'conventional' TIR imaging methods operate, such as TIR fluorescence microscopy, making use of the amplitude changes in fTIR. Amplitude images can also be obtained using digital holography such that outlines of an object in contact on the surface appear as dark areas against bright background, and the darkness would be a measure of the layer thickness z_0.

Case III: It is possible to make use of phase-only changes in fTIR if the angle of incidence is large enough for TIR of both n_1/n_2 and n_1/n_3 interfaces, $\theta_{c,12}, \theta_{c,13} < \theta_1$. Then $h_3 = i\eta_3$ also becomes imaginary and

$$r_\perp = \left(\frac{E_1'}{E_1}\right)_\perp = \frac{(h_1 - i\eta_2)(\eta_2 + \eta_3) + (h_1 + i\eta_2)(\eta_2 - \eta_3)\exp(-2\varphi_0\eta_2)}{(h_1 + i\eta_2)(\eta_2 + \eta_3) + (h_1 - i\eta_2)(\eta_2 - \eta_3)\exp(-2\varphi_0\eta_2)}. \tag{7}$$

Then the reflectance R is identically unity. But in this case, the phase varies with θ_1 and z_0, as seen in Fig. 3 for $74° < \theta_1$, where for z_0 less than a fraction of wavelength, the phase varies monotonically and rapidly. This can be used to provide a sensitive measure of the thickness of the n_2-layer over a range of 100 nm or less.
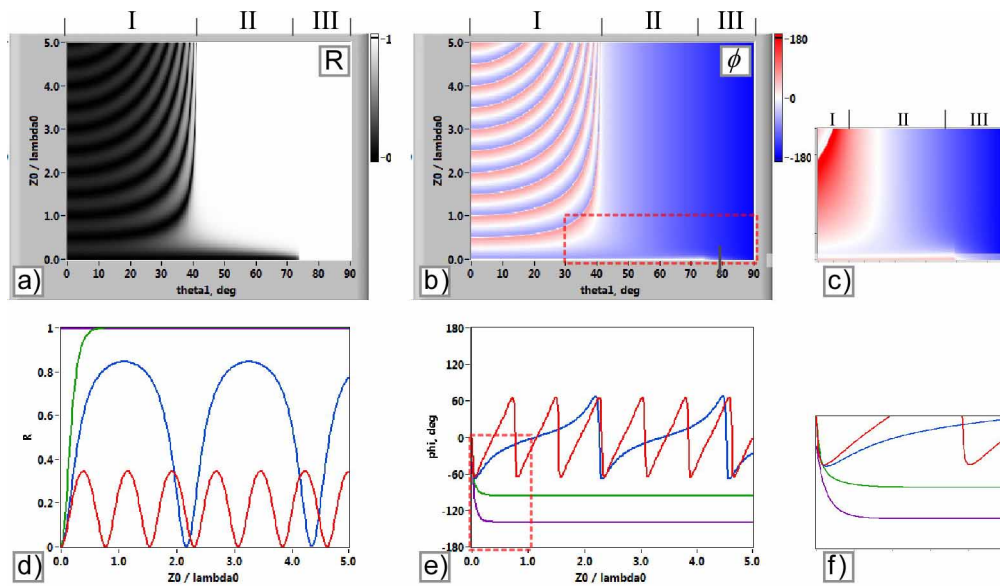

Fig. 3. Reflectance and reflection phase in fTIR, for s-polarization with $n_1 = 1.517$, $n_2 = 1.000$, and $n_3 = 1.458$. a) Reflectance R vs. the angle of incidence, theta1 (θ_1 in text) and the n_2-layer thickness z_0. b) Reflection phase, phi (φ in text) vs. theta1 (θ_1 in text) and z_0. c) Expanded view of the dotted-box area of b). d) Cross-sections of a) at theta1 = $30°$ (red), $40°$ (blue), $60°$ (green), and $75°$ (purple). e) Cross-sections of b) at several values of theta1 (θ_1 in text) as in d). f) Expanded view of the dotted-box area of e).

3. Experiment

Figure 4 shows a basic configuration of the interferometer for digital holographic microscopy of total internal reflection. A yellow HeNe laser ($\lambda = 594$ nm, 2 mW) input beam is split into two parts, object (obj) and reference (ref), by a beam splitter BS1 and recombined at BS2 for superposition, forming a Mach-Zehnder interferometer. The object beam enters the prism and undergoes total internal reflection at the hypotenuse A of the right-angle prism. S-polarization is used in the imaging experiments. The presence of a specimen on the prism surface

modulates the phase front of the reflected light. A objective lens L_{obj} (f = 15 mm, NA = 0.4) placed next to the prism projects a magnified image of the hologram plane H on to the CCD camera, through an imaging optics L_{img}. Another lens L_{ref} is placed in the reference arm so that the two beams have matching wavefront curvatures. The CCD camera (SONY XCD-X710CR, 1034 x 779 pixels, 4.65 x 4.65 μm^2 per pixel) acquires an image of the hologram plane H (which is usually taken in close vicinity of the object plane A) in superposition with the reference beam. A set of programs developed in-house using LabVIEW$^®$ calculates propagation of the optical field back to the object plane A. Because of the presence of the prism, the object plane A optically appears to the camera, or to the plane H, at about 72° angle of inclination, which causes large difference (about 1:3) in the x- and y-scales of images presented below. (This angle is only coincidentally of same numerical value as θ_1 below.) The anamorphism can be compensated for by using an algorithm for numerical diffraction on to an inclined plane [26], but we have not yet implemented it in this proof-of-principle demonstration of TIRHM.
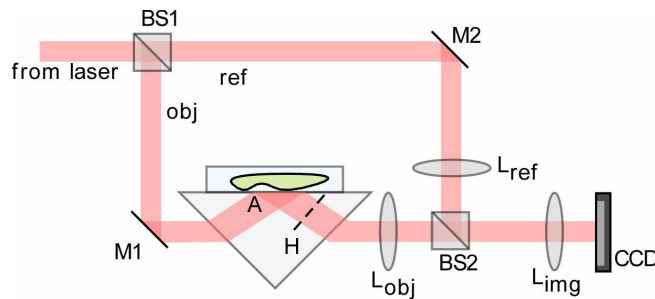

Fig. 4. Apparatus for digital holography of total internal reflection. BS: beam-splitters; M: mirrors; L: lenses; A: object plane; H: hologram plane.

First, we demonstrate the imaging of the reflected phase profile due to variations of refractive index of materials in contact with the prism. As shown in Fig. 5(a), water droplets of index n_2 = 1.333 are placed on the prism of BK7 glass, n_1 = 1.517. Figure 5(b) is the amplitude image of the reflected optical field, while Fig. 5(c) is the phase image, at the object plane A, calculated from a hologram image at H., The field of view is 300 x 900 μm^2 and the presumably circular water droplets, of about 100 μm in diameter, appear highly elliptical because of the relatively large angle of the plane A relative to H. Given the angle of incidence $\theta_1 = 72°$, TIR is in effect for both glass-air and glass-water interfaces. The amplitude image of Fig. 5(b) does show variations in intensity due to diffraction from phase discontinuities and other spurious interference. We note that when the angle of incidence is not large enough for TIR at the glass-water interface, the water droplets appear as black spots because of the diminished reflectance. On the other hand, the phase image of Fig. 5(c) has significantly less noise or spurious signal and displays the profile of water droplets with good fidelity. Referring to Fig. 1(c), the reflection phase shift is $\varphi = -131°$ for the glass/air interface, while it is $\varphi = -97°$ for the glass/water interface, so that the phase difference between the two areas is expected to be $\Delta\varphi = 34°$. Figure 5(d) is a cross-section through one of the droplets of Fig. 5(c), where the phase step is measured to be about $\Delta\varphi = 40° \pm 5°$. A similar measurement is made using 50/50 mixture of water (1.333) and ethylene glycol (1.432) in Fig. 5(e). With presumed index of 1.382 for the mixture, the expected phase step is $\Delta\varphi = 85°$, while the measured value is $\Delta\varphi = 60° \pm 10°$. Although these numerical values have significant uncertainties, the trend is consistent with expectation, i.e., the larger the index difference, the larger the phase difference.
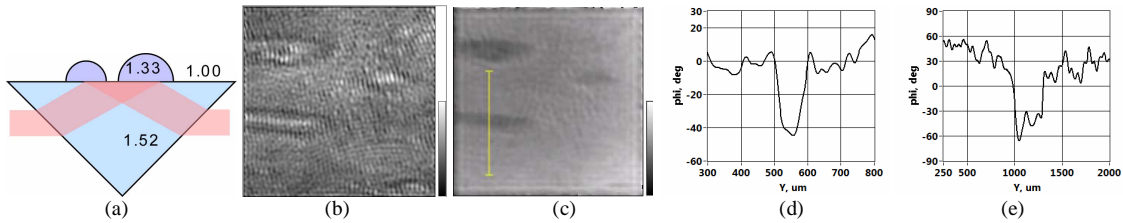
Fig. 5. (a). General configuration of water droplets placed on prism. b) Amplitude and c) phase images of light reflected from the prism detailing cross-section cut line. Field of view is approximately 300 x 900 μm^2 with 256 x 256 pixels. Gray scale for b) is 0 ~ 1 in arbitrary unit, while for c) it is $-180° \sim +180°$. d) Graph of cross-section along a vertical line through a water drop in c). e) A similar graph for a droplet of 50/50 mixture of water and ethylene glycol.

The next experiment demonstrates imaging of phase profile resulting from variation of thickness of the gap between two layers of materials. As depicted in Fig. 6(a), a fused quartz plano-convex lens (n_3 = 1.458) of UV focal length 250 mm is placed on the glass (n_1 = 1.517) prism. Note that only the index of refraction (at visible wavelength) and the surface curvature of the sample lens are the pertinent parameters for this experiment, while the UV focal length is not. The angle of incidence was 75°, just beyond the critical angle of glass-quartz interface ($\theta_{c,13} = 74°$). The relatively uniform amplitude image in Fig. 6(b) indicates TIR, whereas the phase image in Fig. 6(c) shows a clear profile of the contact area (which again has about 3:1 anamorphism). The field of view is 260 μm horizontal by 780 μm vertical. The radius of curvature of the convex surface is 115 mm, so that the air gap (n_2 = 1.000) goes from zero at the point of contact to 660 nm at the edge of the 780 μm vertical field of view.
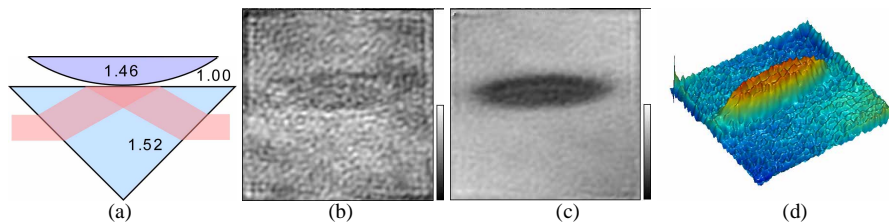

Fig. 6. (a). General configuration of quartz lens placed on prism. b) Amplitude and c) phase images of light reflected from the prism. d) Pseudo-color perspective rendering of c). Field of view is approximately 260 x 780 μm^2 with 256 x 256 pixels. Gray scale for b) is 0 ~ 1 in arbitrary units, while for c) it is $-180° \sim +180°$.

A cross-section of Fig. 6(c) along a vertical line through the center of the spot is shown in Fig. 7(a), while Fig. 7(d) shows such cross-section calculated from the given indices and curvature. The measured phase dip through the spot is $130° \pm 15°$, while the modeled value is 100°. The discrepancy is attributed to spurious diffraction and other interference. The spot in the phase image Fig. 6(c), or its pseudo-color perspective rendering in Fig. 6(d), represents the area of contact, circular shape of about 140 μm diameter and within 20 nm between the prism and lens surfaces. That is, the thickness of the evanescent field is about 20 nm and the profile of the lens surface within the evanescent field can be imaged. The measurements are repeated by filling the glass-quartz gap with 50/50 mixture of water and ethylene glycol (n_2 = 1.382, Figs. 7(b) and 7(e)), and with pure ethylene glycol (n_2 = 1.432, Figs. 7(c) and 7(f)).
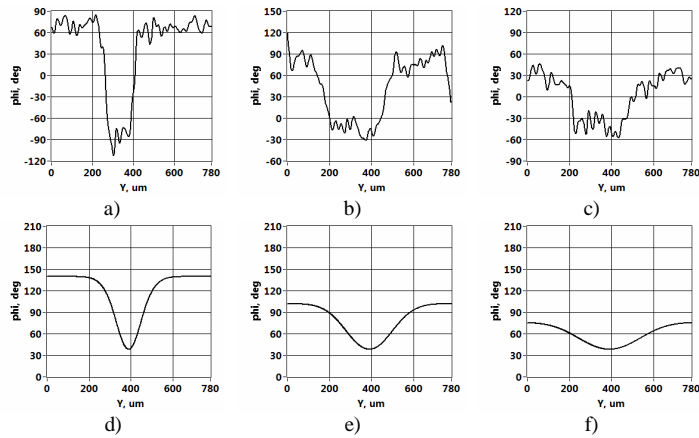
Fig. 7. Cross-section of phase profile across the contact spot of quartz lens on glass prism, when the gap is filled with a) air, b) 50/50 mixture of water and ethylene glycol, and c) pure ethylene glycol. Panels d), e), and f) are the corresponding theoretical graphs.

The expected phase dips for these cases are $60°\pm15°$ and $35°\pm15°$, while the measured values are $80°$ and $50°$, respectively. These measured values of phase dips as well as the width of the spots show trends consistent with the model. When the gap is filled with these materials, the index difference across interfaces become smaller and the evanescent fields become thicker. The maximum gaps that can be imaged in these cases are 70 nm and 120 nm, respectively.

4. Discussion and conclusions

We have introduced a novel microscopy method of total internal reflection holographic microscopy (TIRHM) for obtaining quantitative phase images of light in total internal reflection (TIR). The theory of TIRHM is developed from the basic Fresnel description of TIR and frustrated TIR (fTIR). Phase shifts in TIR and fTIR are calculated in terms of the indices of refraction, angle of incidence, and the gap thickness. Digital holography allows imaging of the phase profile of TIR and two specific imaging modes of TIRHM are described. In one, the reflection phase profile results from variation of refractive index of an object of inhomogeneous optical property in contact with the prism. A biological cell, for example, in complete contact with the prism surface can be imaged to reveal the intracellular structure. In the other mode, the reflection phase profile images the gap distance between the surfaces of the prism and an object placed on the prism. For example, a biological cell in locomotion can reveal the profile of protrusion of pseudopodia, formation of focal adhesion, development of traction, and release of adhesion.

The holographic microscopy of total internal reflection (TIRHM) is particularly advantageous in cellular microscopy applications for a number of reasons. The imaging makes use of total reflection, meaning essentially all of the input photons participate in the formation of the image signals, and therefore the input optical power can be kept at minimal level. Although the intensity images of conventional holography are often associated with speckle and other interference noise, the phase images of digital holography are much less susceptible to such noise. The phase image is directly calculated from the hologram as part of the complex optical field. Therefore it is completely quantitative and can be subjected to various numerical processing techniques. In principle, it may be possible to image the phase front of TIR using conventional interference techniques, but the geometry of the imaging system through the prism requires the ability to image a plane with large inclination angle. This is not possible in any existing microscopy technology, whereas digital holography has a great deal of flexibility including the ability to image an inclined plane. With a relatively simple apparatus, one can easily obtain phase images of prism-cell interface with a optical

thickness resolution of a few nanometers. We have demonstrated these imaging principles of TIRHM using model objects of liquid droplets and spherical surface of known material and shape. The results unambiguously demonstrate the capabilities of TIRHM to image profiles of these parameters and indicate strengths in potential applications in biomedical cellular imaging.

Acknowledgments